OPTOELECTRONICS AND ADVANCED MATERIALS – RAPID COMMUNICATIONS Vol. 16, No. 11-12, November-December 2022, p. 491 - 500

Design and analysis of beam splitter based on all-dielectric encoding metasurface

JUNLING HAN*
Jinan Vocational College, Jinan, China

Metal-based beam splitters limit device efficiency. In order to improve the beam splitter efficiency and reduce the ohmic loss of metal materials, we propose to use all-dielectric materials to design a terahertz beam splitter. Moreover, it is an effective way to design beam splitters using all-dielectric metamaterial structures. With the rapid development of digital technology, it is difficult for traditional analog metamaterials to digitally control electromagnetic information. We propose the use of encoded metamaterial structures to realize the design of terahertz beam splitters. Different encoding modes can control different scattering angles of the beam splitter. Using all-dielectric encoding metasurfaces, we design a transmissive terahertz beam splitter and a reflective beam splitter. It is generally believed that the design of reflective beam splitters requires a metal layer to improve the reflection efficiency, however, the loss of metal materials is also inevitable. We use the all-dielectric encoded metamaterial structure to design a reflective beam splitter, which makes it possible to use the all-dielectric structure to design a reflective device.

(Received June 21, 2022; accepted December 5, 2022)

Keywords: Metasurface, Splitter, Encoding

1. Introduction

Beam splitters are indispensable components in various optical applications such as interferometers, multiplexers, etc. They play an important role in the communication transmission system. The structure of the traditional beam splitter device is relatively cumbersome and cannot realize the free control of the beam. Traditional beam splitters are not conducive to miniaturization, integration and multidirectional transmission characteristics. The study of metamaterial structure has attracted great attention [1-10]. Metamaterials usually refer to artificial composite structures or composite materials with exotic electromagnetic properties that are not found in natural materials [11-20]. Researchers can rationally optimize the cell structure and cell size, and artificially design exotic electromagnetic properties. Metamaterials are widely used in microwave, terahertz, infrared and visible light range [21-30]. Metamaterials can be used in wireless communications, radar, stealth, imaging, negative refraction, and perfect lenses [31-40].

Terahertz waves are highly penetrating and can pass through wood, plastic and ceramics, enabling perspective imaging of opaque objects. Compared with microwaves, terahertz waves have higher spatial resolution and can be used to distinguish the appearance and composition of objects. When terahertz waves irradiate an object, the morphological structure of its molecules will not be changed, and it can be used for non-destructive testing. Terahertz beam splitters are very important devices in terahertz systems. For example, V. Chheang et al. proposed a compact terahertz polarization beam splitter based on a multimode interference structure [41]. Gao et al. proposed an ultra-broadband Y-shaped terahertz beams plitter [42], which consists of a straight waveguide based on an H-shaped structure and two branched waveguides, and its straight and branched waveguides have similar dispersion relations and mode properties. J. Shibayama et al. proposed a terahertz beam splitter based on radial grating structure [43]. Lai et al. proposed a terahertz beam splitter based on a silicon-based antiferromagnetic nanofilm, which can split the incident wave into two beams [44]. However, the research on terahertz beam splitters mainly focuses on the structure of metal materials. Ohmic losses of metal materials seriously affect device efficiency. In order to improve the device efficiency, it is possible to use all-dielectric materials to design terahertz beam splitters. Compared with metal metasurface, all-medium metasurface beam splitter can provide relatively high transmission efficiency, especially in visible and near-infrared bands. It can also be designed as all-medium monolayer structure, making the experimental preparation process more simple. The all-dielectric unit structure can achieve both electrical resonance and magnetic resonance, while for metal structure, multi-layer structure is needed to achieve magnetic resonance. Moreover, the low cost of raw materials and compatibility with advanced semiconductor processes allow all-dielectric metasurface beam splitters to be integrated into photonic systems.

Here, we design transmissive and reflective THz beam splitters using all-dielectric metamaterials. With the rapid

development of digital technology, it is difficult for traditional analog metamaterials to digitally control electromagnetic information. Using the all-dielectric cylindrical structure, different coding units are designed and obtained. We utilize different coding modes to achieve control of the scattering angle of the transmissive and reflective beam splitters.

2. Beam splitter scattering theory of metasurface

Digitally encoded metasurfaces use digital states to characterize electromagnetic parameters, directly linking digital technology at the information level with metasurface technology at the physical level. The 1-bit metasurface consists of two cell structures with a phase difference of 180°, corresponding to the binary numbers "0" and "1". Far-field beam splitting scattering properties of coding metasurfaces are obtained based on phased array antenna theory. If there are m*n coding units to form a coding metasurface, "0" units and "1" units are alternately arranged in the plane coordinates, and the size of each unit is the same, which is T, then the coding metasurface is in the plane coordinates. The period in both directions is 2T. The transmitted or reflected phase of each cell is marked as $\Phi(\mathrm{m},\mathrm{n})$. According to the principle of phased array antenna, the far-field scattering of the transmitted wave can be expressed as [45]

$$F(\theta,\varphi) = \sum_{m=1}^{M}\sum_{n=1}^{N} T_{m,n} e^{-i(kd_x\left(m-\frac{1}{2}\right)\sin\theta\cos\varphi + kd_y\left(n-\frac{1}{2}\right)\sin\theta\sin\varphi)} \quad (1)$$

where $T_{m,n}$ shows the transmitted coefficient for encoding unit, k is wave vector, and θ and φ are elevation and azimuth angles of scattering. It is assumed that the transmission coefficient of each coding unit is 1, and the phase of each coding unit is 0 or π. Equation (1) can be simplified as

$$F(\theta,\varphi) = \sum_{m=1}^{M} e^{-i(kd_x\left(m-\frac{1}{2}\right)\sin\theta\cos\varphi + m\pi)} \sum_{n=1}^{N} e^{-i(kd_y\left(n-\frac{1}{2}\right)\sin\theta\sin\varphi + n\pi)} \quad (2)$$

We can further obtain as

$$|F(\theta,\varphi)| = MNSinc\left(m\pi\left(p+\frac{1}{2}\right) - \frac{m}{2}kd_x\sin\theta\cos\varphi\right) Sinc\left(n\pi\left(q+\frac{1}{2}\right) - \frac{n}{2}kd_y\sin\theta\sin\varphi\right), \quad (3)$$

where p, q=0, ±1, ±2.... It can be deduced from Eq. (3) that $|F(\theta,\varphi)|$ reaches its first extreme value, when it satisfy the following conditions as

$$\varphi = \pm tan^{-1}\frac{d_x}{d_y}, \varphi = \pi \pm tan^{-1}\frac{d_x}{d_y}, \quad (4)$$

$$\theta = sin^{-1}\left(\frac{\pi}{k}\sqrt{\frac{1}{d_x^2}+\frac{1}{d_y^2}}\right). \quad (5)$$

When $\Gamma_x = 2d_x$, $\Gamma_y = 2d_y$, and $k = 2\pi/\lambda$, Eq.(7) can be simplified as

$$\theta = sin^{-1}\left(\lambda\sqrt{\frac{1}{\Gamma_x^2}+\frac{1}{\Gamma_y^2}}\right). \quad (6)$$

Γ_x and Γ_y indicate the super period of encoding metasurface in *x*-direction and *y*-direction, respectively. If $\Gamma_x \to \infty$, or $\Gamma_y \to \infty$, Eq.(6) for the elevation angle θ of the anomalous beam can be simplified as

$$\theta = sin^{-1}\left(\frac{\lambda}{\Gamma}\right), \quad (7)$$

where Γ indicates coding period in the encoding direction.

3. Transmissive all-dielectric beam splitter

According to the generalized Snell's law, if one wants to control the transmitted wave to emerge at any angle, it can be achieved by designing and changing the phase gradient imposed on the metasurface. If the phase gradient has two diametrically opposite directions at the metasurface interface, then the transmitted wave would split and refract and exit in two directions. The control principle of the metasurface beam splitter is to introduce abrupt phase to control the transmission phase, and then control the change of the transmission phase by changing the periodic arrangement of the abrupt phase, making it possible to manipulate the beam splitting angle and splitting ratio of the outgoing wave.

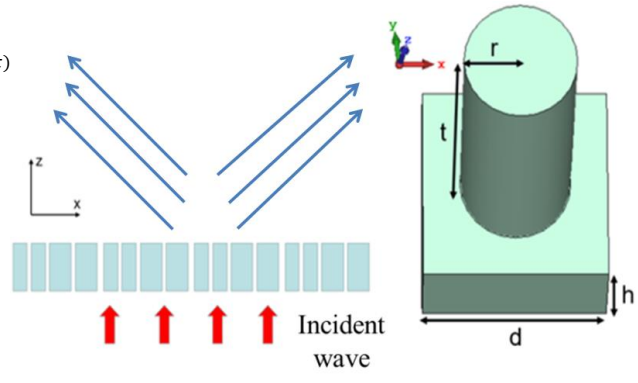

Fig. 1. Schematic diagram of coding metasurface beam splitter and schematic diagram of unit structure (color online)

First, we design a transmissive all-dielectric-encoded metasurface beam splitter. The beam splitter adopts a variety of periodically arranged silicon dielectric column structures, mainly to provide the abrupt phase of the transmission wave splitting and refraction through a non-uniform arrangement. As shown in Fig. 1, an arrangement structure is shown, and the abnormal refraction characteristics mainly depend on the size of the unit structure and the periodic arrangement. In order to realize terahertz metasurface demultiplexing, we choose two kinds of all-silicon dielectric cylinders with different radius and length. The terahertz all-dielectric transmission beam splitter unit structure consists of a substrate and a cylinder on the substrate, and the entire structure uses silicon material. The substrate is composed of a square with a length of d and a thickness of h, and the silicon material cylinder on the substrate has a radius of r and a height of t. The right figure in Fig. 1 shows the structure of the all-silicon dielectric unit. Due to the high transmittance and refractive index of the silicon medium in the terahertz wave band, efficient Fabry-Perot resonance can be achieved in the cylinder. Thus, an appropriate phase delay can be introduced to the transmitted wave. The required phase delay can be achieved by changing the cylinder radius. We used the finite-difference time-domain method to optimize the design. After optimized design, the structural parameters of the beam splitter are of d = 100 μm, h = 50 μm, and t = 150 μm. And two unit cells with the different cylinder radius r can be designed as r1 = 28.5 μm and r2 = 47 μm. The cylinder material is Si with a dielectric constant εr of 11.9, loss angle tangent of 0.0357 and refractive index of 3.45. Fig. 2 shows the transmission amplitude and transmission phase for these two cell structures of different radii. There are two sharp transmission dips near the 1THz frequency. This may be caused by the guided mode resonance effect. In the diffracted light field, the energy distribution of light wave is reproduced due to the coupling resonance after mode matching between the high-order diffracted wave generated by the grating modulation and the mode leaked by the waveguide. In this way, very sharp resonant peaks appear at some wavelengths. At the frequency of 0.8 THz, the transmission amplitude of the two unit structures is relatively high, and the transmission phase difference is close to 180 degrees. Therefore, we can use these two unit structures to construct a 1-bit encoding metasurface to achieve beam splitting properties.

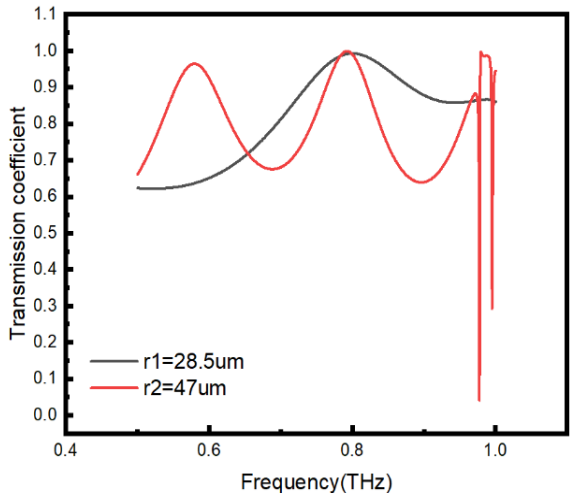

(a)

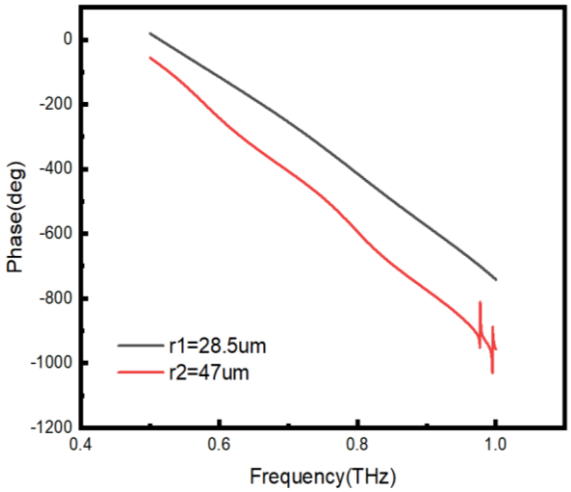

(b)

Fig. 2. Transmission amplitude (a) and transmission phase (b) (color online)

To verify the effect of the fully adjustable beam splitting angle of the terahertz all-dielectric beam splitter, we utilize the two previously designed cell structures to construct encoded metasurfaces with different periods. Fig. 3(a) shows a schematic diagram of an encoded metasurface with a period of 400 μm. The corresponding far-field scattered beam splitting characteristics are shown in Fig. 3(b). For the surface metasurface arrangement with a period of 400 μm, the two beam scattering directions of the corresponding far-field beam splitting are deflected along the negative x-axis and the positive x-axis, respectively. Based on the far-field scattering principle of the encoding metasurface, using formula (3), we can calculate that the two beams of transmitted light along an angle of 69 degrees. The above numerical simulation results are basically consistent with the theoretical calculation results. At the same time, the deflection angle and light intensity of the two beams emitted by the beam splitter are different, which may be caused by the interaction between the unit structures.

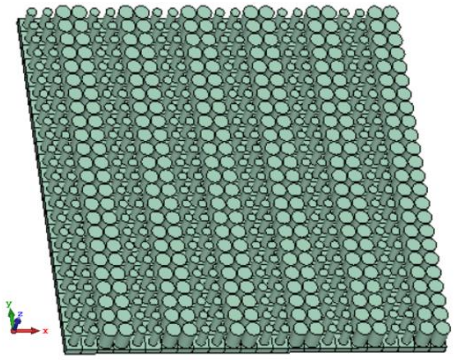

(a)

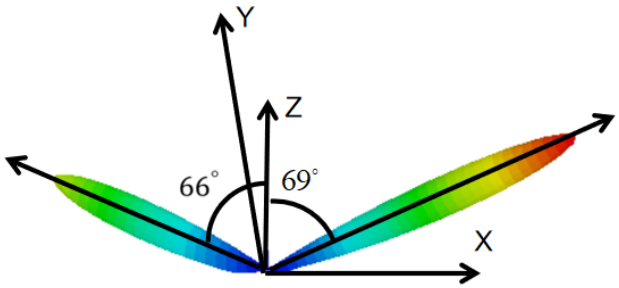

(b)

Fig. 3. (a) Schematic representation of an encoded metasurface with a period of 400 μm. (b) The corresponding far-field scattered beam splitting characteristics (color online)

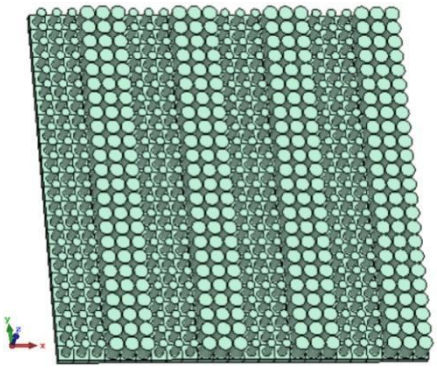

(a)

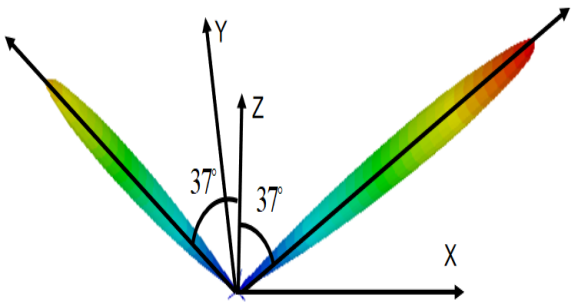

(b)

Fig. 4. (a) Schematic representation of an encoded metasurface with a period of 600 μm. (b) The corresponding far-field scattered beam splitting characteristics (color online)

To further confirm that the encoding metasurface can control different beam angles, we designed the encoding metasurface sequence with a period of 600 μm, as shown in Fig. 4(a). The corresponding two scattered beams are shown in Fig. 4(b). The numerically simulated scattering angle of the two beams is 37°. According to the far-field scattering theory and Equation 3, we can theoretically calculate the scattering angle of this encoding sequence to be 38°. The theoretical calculation results are basically consistent with the numerical simulation results. The error between the two is about 1°. This error may be caused by the interaction between coding units and the small number of computational units. In order to further adjust the scattering angle, we designed an encoding metasurface sequence with an encoding period of 800 μm, as shown in Fig. 5(a). The corresponding far-field scattering is shown in Fig. 5(b). The numerically simulated scattering angle of the two beams is 27°. According to the far-field scattering theory and Equation 3, we can theoretically calculate the scattering angle of this encoding sequence to be 28°. The theoretical calculation results are basically consistent with the numerical simulation results.

To demonstrate the splitting properties of multiple beams in 3D space, we further design a checkerboard encoding pattern, as shown in Fig. 6(a). Next, two checkerboard coding modes with the same cell structure described above, but with different periodic arrangements, are introduced. The arrangement of the checkerboard coding is to evenly arrange the silicon cylinders of different radius lengths together, which can effectively reduce the interaction between different unit structures, and most importantly, can obtain the splitting characteristics of multiple beams in 3D space. The corresponding 3D spatial far-field scattered beams are shown in Fig. 6(b). As shown in the figure, a metasurface beam splitter with a periodic arrangement of four units divides the transmitted light perpendicularly incident from the substrate into four outgoing beams. The deflection angle of the numerically simulated beamless beam is 66°. According to equation (6), we can theoretically calculate the scattering angle of this checkerboard encoding pattern to be 69°. The numerical simulation results are basically consistent with the theoretical calculation results. To fully demonstrate that the deflection angles of the four beams in three-dimensional space can be adjusted freely, we further design a checkerboard-encoded pattern metasurface with different periods, as shown in Fig. 7(a). The corresponding far-field scattering distribution is shown in Fig. 7(b). According to the numerical simulation results, we can see that the far-field scattering angle is 14°. According to the

theoretical calculation and equation (6), we can theoretically calculate that the scattering angle is 13°. The errors of the theoretical calculation results and the numerical simulation results are reduced relative to the results in Fig. 6. This is due to the increase in the number of repetitions of each coding unit in a cycle of this checkerboard coding pattern, resulting in a decrease in the interaction between the unit structures, which further makes the numerical simulation and theoretical calculation more consistent.

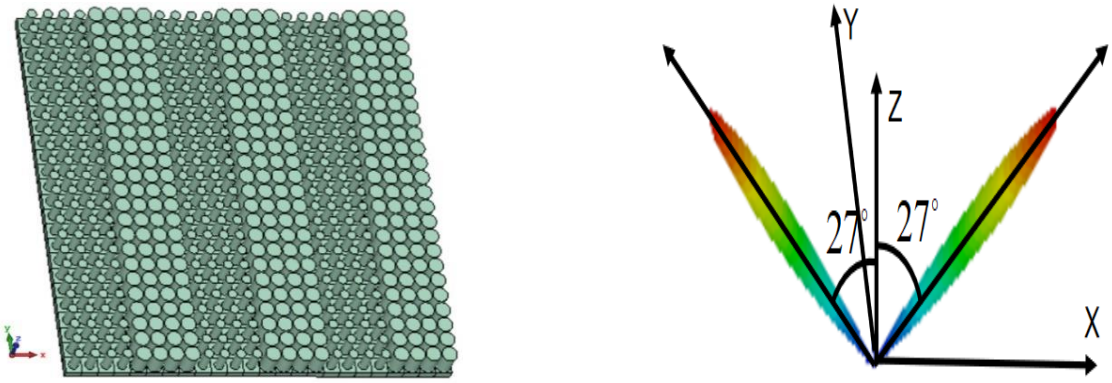

(a) (b)

Fig. 5. (a) Schematic representation of an encoded metasurface with a period of 800 μm. (b) The corresponding far-field scattered beam splitting characteristics (color online)

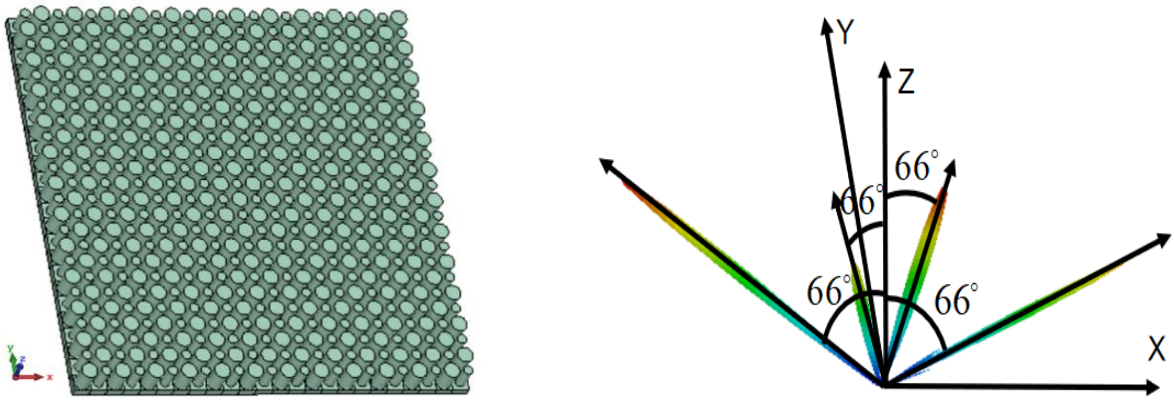

(a) (b)

Fig. 6. (a) Schematic of an encoded metasurface with the checkerboard encoding mode and the period of 200 μm. (b) The corresponding far-field scattered beam splitting characteristics (color online)

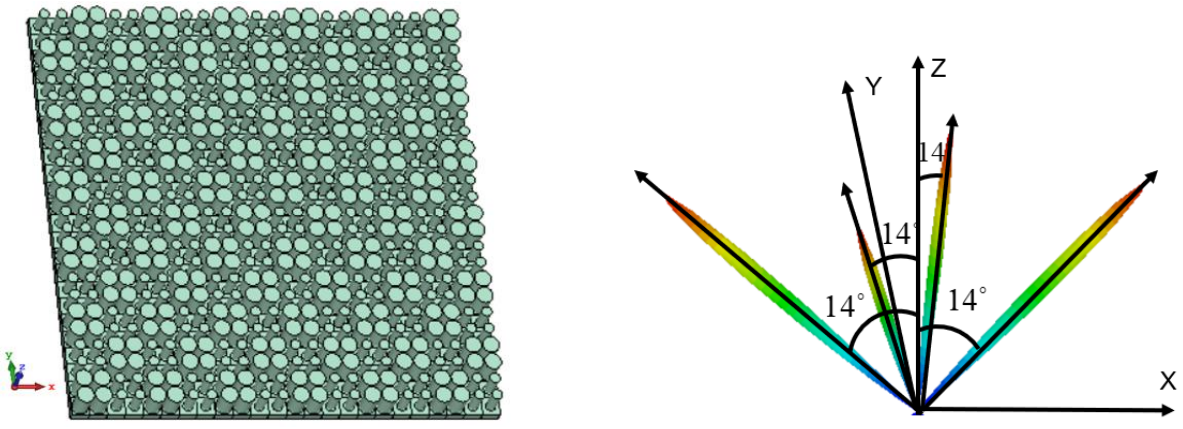

(a) (b)

Fig. 7. (a) Schematic of an encoded metasurface with the checkerboard encoding mode and the period of 400 μm. (b) The corresponding far-field scattered beam splitting characteristics (color online)

4. Reflective all-dielectric beam splitter

We have designed the transmission beam splitter in detail above. In general, the all-dielectric unit structure is generally considered to be mainly used in the design of transmissive devices. However, there are few reports on all-dielectric material units for designing reflective devices. It is generally believed that a reflective device needs to be designed with a metal reflective layer. However, due to the ohmic loss of the metal material, the device efficiency is greatly reduced. In order to reduce the loss characteristics of metal materials and improve the efficiency of the device, we further use the all-dielectric unit structure to design a reflective encoding metasurface beam splitter.

To achieve the required reflective phase delay can be achieved by changing the cylinder radius. After optimized design, the structural parameters of the beam splitter are of d = 100 μm, h = 50 μm, and t = 180 μm. And two unit cells with the different cylinder radius r can be designed as r1 = 20 μm and r2 = 35 μm. Fig. 8 shows the reflective amplitude and reflective phase for these two cell structures of different radii. At the frequency of 1.4 THz, the reflective amplitude of the two unit structures is relatively high, and the reflective phase difference is close to 180 degrees. Therefore, we can use these two unit structures to construct a 1-bit encoding metasurface to achieve beam splitting properties for reflection mode.

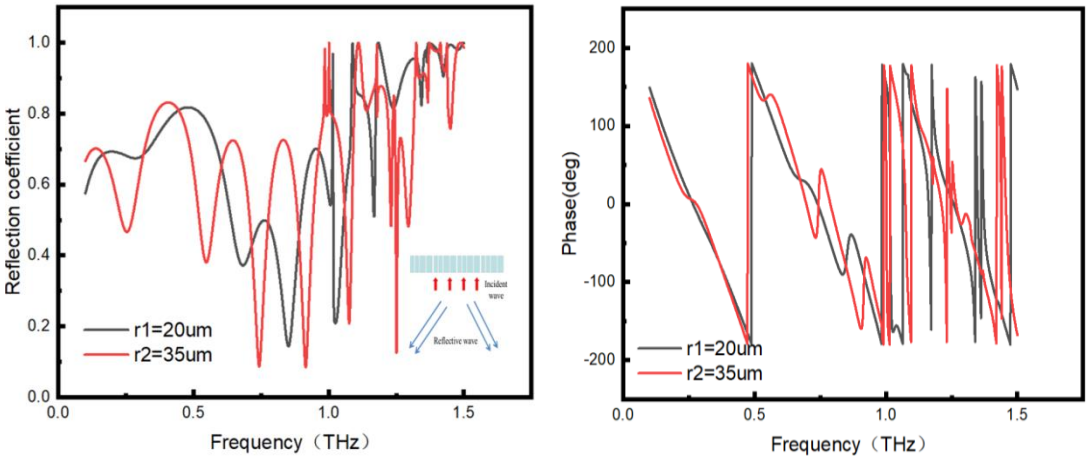

(a) (b)

Fig. 8. Reflective amplitude (a) and reflective phase (b) (color online)

To verify the effect of the fully adjustable beam splitting angle of the reflective all-dielectric beam splitter, we utilize the two designed cell structures to construct reflective encoded metasurfaces with different periods. Fig. 9(a) shows a schematic diagram of an encoded metasurface with a period of 400 μm. The corresponding far-field scattered beam splitting characteristics are shown in Fig. 9(b). For the surface metasurface arrangement with a period of 400 μm, the two beam scattering directions of the corresponding far-field beam splitting are deflected along the negative x-axis with 30 degree and the positive x-axis with 31 degree, respectively. Based on the far-field scattering principle of the encoding metasurface, using formula (3), we can calculate that the two beams of transmitted light along an angle of about 32 degree. The above numerical simulation results are basically consistent with the theoretical calculation results. At the same time, the deflection angle and light intensity of the two beams emitted by the beam splitter are different, which may be caused by the interaction between the unit structures.

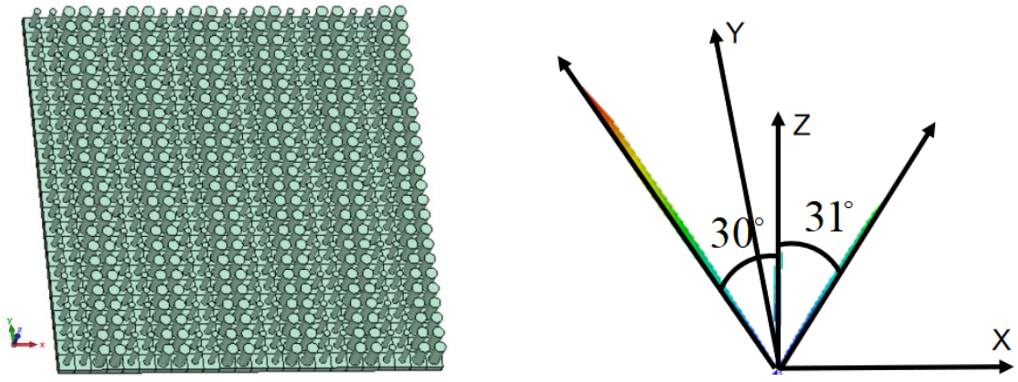

(a) (b)

Fig. 9. (a) Schematic representation of an reflective encoded metasurface with a period of 400 μm. (b) The corresponding far-field scattered beam splitting characteristics (color online)

To further confirm that the reflective encoding metasurface can control different beam angles, we designed the encoding metasurface sequence with a period of 600 μm, as shown in Fig. 10(a). The corresponding two scattered beams are shown in Fig. 10(b). The numerically simulated scattering angle of the two beams is about 20°. According to the far-field scattering theory and Equation 3, we can theoretically calculate the scattering angle of this encoding sequence to be 21°. The theoretical calculation results are basically consistent with the numerical simulation results. The error between the two is about 1°.

In order to further adjust the reflective scattering angle, we designed an encoding metasurface sequence with an encoding period of 800 μm, as shown in Fig. 11(a). The corresponding far-field scattering is shown in Fig. 11(b). The numerically simulated scattering angle of the two beams is 17°. According to the far-field scattering theory and Equation 3, we can theoretically calculate the scattering angle of this encoding sequence to be 15°. The theoretical calculation results are basically consistent with the numerical simulation results.

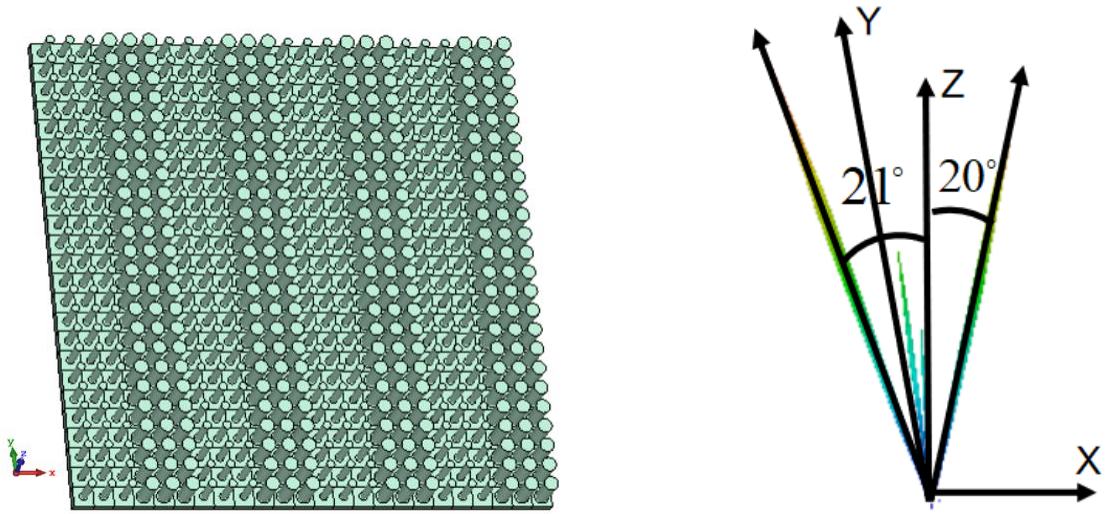

(a) (b)

Fig. 10. (a) Schematic representation of an reflective encoded metasurface with a period of 600 μm. (b) The corresponding far-field scattered beam splitting characteristics (color online)

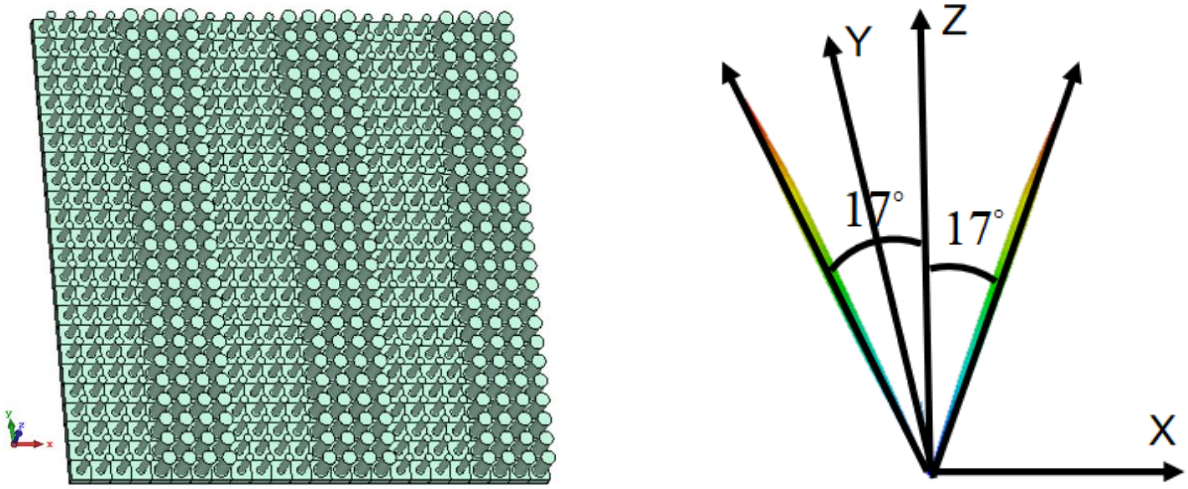

(a) (b)

Fig. 11. (a) Schematic representation of an reflective encoded metasurface with a period of 800 μm. (b) The corresponding far-field scattered beam splitting characteristics (color online)

To demonstrate the splitting properties of multiple reflective beams in 3D space, we further design a checkerboard encoding pattern, as shown in Fig. 12(a). The corresponding 3D spatial far-field scattered beams are shown in Fig. 12(b). The deflection angle of the numerically simulated beams is 31°. According to equation (6), we can theoretically calculate the scattering angle of this checkerboard encoding pattern to be 32°. The numerical simulation results are basically consistent with the theoretical calculation results. To fully demonstrate that the deflection angles of the four beams in three-dimensional space can be adjusted freely, we further design a checkerboard-encoded pattern metasurface with different periods, as shown in Fig. 13(a). The corresponding far-field scattering distribution is shown in Fig. 13(b). According to the numerical simulation results, we can see that the far-field scattering angle is 7°. When we designed the separation of the double beams, the separation of the two beams is obvious. However, for the multi-beam splitting, there seemed to be a lot of sidelobes. This is probably because when we designed the split of the two beams, we arranged as many cycles as possible given the computational power. However, when we design multi-beam splitting, the total number of units we design is fixed due to the limitation of computing power. The cycle size of multi-beam splitting units is relatively large, which leads to a small number of permutation cycles. This results in multiple side lobes. The beam splitter we designed may be applied to other fields [46-53]. Even though the presented work is fully based on numerical simulations of encoding metasurfaces, it is feasible to prepare such all dielectric encoding metasurfaces. The preparation processes include the base bonding, the conventional mask photolithography, and the Bosch deep reactive ion etching process.

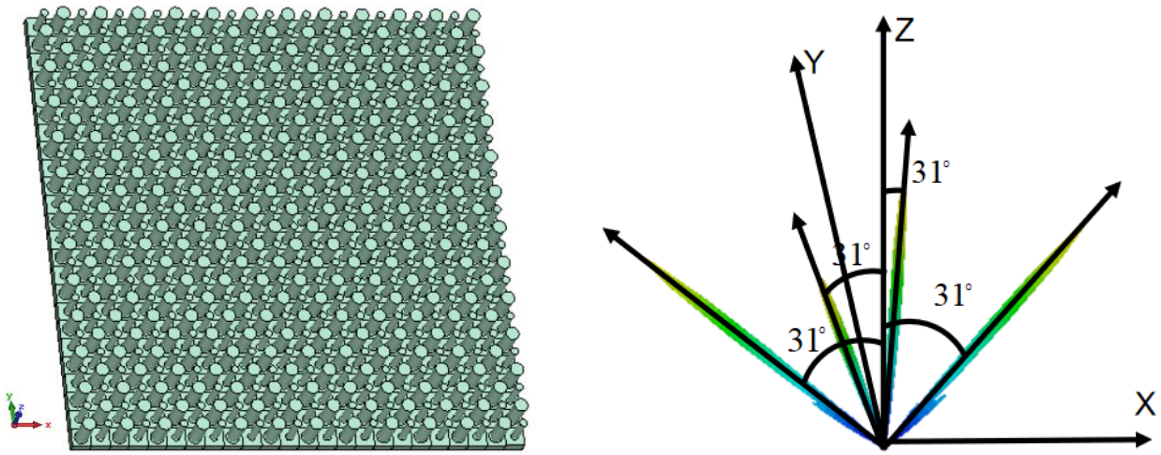

(a) (b)

Fig. 12. (a) Schematic of an reflective encoded metasurface with the checkerboard encoding mode and the period of 200 μm. (b) The corresponding far-field scattered beam splitting characteristics (color online)

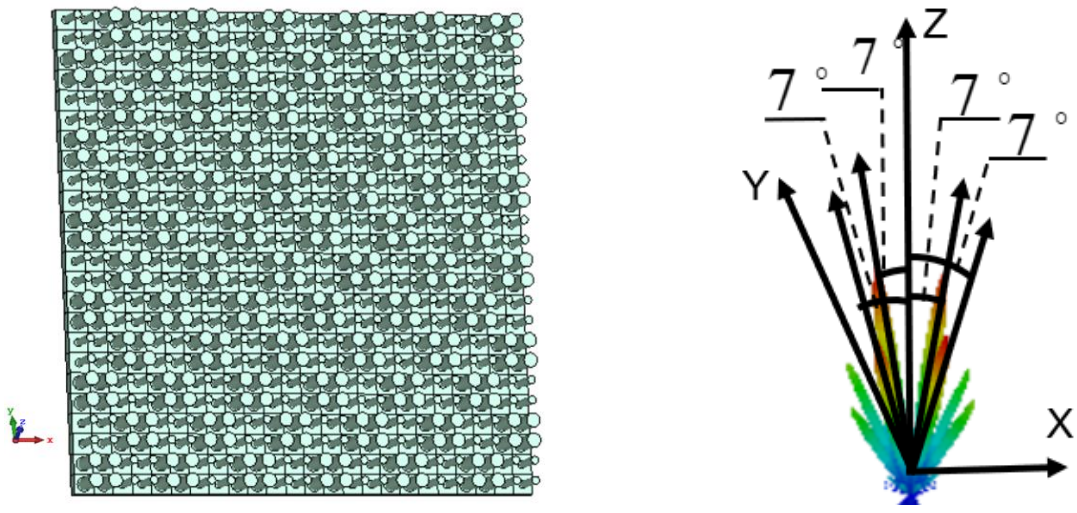

(a) (b)

Fig. 13. (a) Schematic of an reflective encoded metasurface with the checkerboard encoding mode and the period of 400 μm. (b) The corresponding far-field scattered beam splitting characteristics (color online)

5. Conclusions

As an important terahertz device, the terahertz beam splitter is widely used in various fields such as terahertz band communication and imaging. Compared with other structures, devices with metasurface structures have the advantages of being simpler and more specific and flexible in design. In this paper, a transmissive all-silicon dielectric-encoded metasurface beam splitter and a reflective all-silicon dielectric-encoded metasurface beam splitter are designed. Both can provide a 1-bit phase change in the terahertz band by changing the different radii of the silicon pillars on the base of their unit structure. By changing the periodic arrangement law of different unit structures, the control of changing the splitting angle of the outgoing beam is achieved.

References

[1] X. He, Carbon **82**, 229 (2015).
[2] X. He, X. Zhong, F. Lin, W. Shi, Opt. Mater. Express **6**, 331 (2016).
[3] Xiaoyong He, Feng Liu, Fangting Lin, Wangzhou Shi, Opt. Lett. **46**, 472 (2021).
[4] Xiaoyong He, Feng Liu, Fangting Lin, Wangzhou Shi, J. Phys. D: Appl. Phys. **54**, 235103 (2021).
[5] Jun Peng, Xiaoyong He, Chenyuyi Shi, Jin Leng, Fangting Lin, Feng Liu, Hao Zhang, Wangzhou Shi, Physica E **124**, 114309 (2020).
[6] X. Jing, S. Jin, Y. Tian, P. Liang, Q. Dong, L. Wang, Optics & Laser Technology **48**, 160 (2013).
[7] X. Jing, Y. Xu, H. Gan, Y. He, Z. Hong, IEEE Access **7**, 144945 (2019).
[8] L. Jiang, B. Fang, Z. Yan, J. Fan, C. Qi, J. Liu, Y. He, C. Li, X. Jing, H. Gan, Z. Hong, Optics & Laser Technology **123**, 105949 (2020).
[9] H. Lv, X. Lu, Y. Han, Z. Mou, S. Teng, Optics Letters **44**(10), 2518 (2019).
[10] H. Wang, L. Liu, C. Zhou, J. Xu, M. Zhang, S. Teng, Y. Cai, Nanophotonics **8**(2), 317 (2019).
[11] Jinxing Li, Yueyi Yuan, Qun Wu, Shah Nawaz Burokur, Kuang Zhang, Chin. Opt. Lett. **19**, 100501 (2021).
[12] S. Teng, Q. Zhang, H. Wang, L. Liu, H. Lv, Photonics Research **7**(3), 246 (2019).
[13] M. R. Akram, G. Ding, K. Chen, Y. Feng, W. Zhu, Advanced Materials **32**, 1907308 (2020).
[14] J. Zhang, X. Wei, I. D. Rukhlenko, H.-T. Chen, W. Zhu, ACS Photonics **7**(1), 265 (2020).
[15] Haoyu Wang, Zhiyu Zhang, Kun Zhao, Wen Liu, Pei Wang, Yonghua Lu, Chin. Opt. Lett. **19**, 053601 (2021).
[16] Bo Fang, Zhiyu Cai, Yandong Peng, Chenxia Li, Zhi Hong, Xufeng Jing, Journal of Electromagnetic Waves and Applications **33**(11), 1375 (2019).
[17] B. Fang, B. Li, Y. Peng, C. Li, Z. Hong, X. Jing, Microw. Opt. Technol. Lett. **61**, 2385 (2019).
[18] Weimin Wang, Xufeng Jing, Jingyin Zhao,Yinyan Li,Ying Tian, Optica Applicata **47**(2), 183 (2017).
[19] L. Jiang, B. Fang, Z. Yan, C. Li, J. Fu, H. Gan, Z. Hong, Microwave and Optical Technology Letters **62**(6), 2405 (2020).
[20] Yi Zhao, Qiuping Huang, Honglei Cai, Xiaoxia Lin, Hongchuan He, Hao Cheng, Tian Ma, Yalin Lu, Chin. Opt. Lett. **19**, 073602 (2021).
[21] Hafiz Saad Khaliq, Inki Kim, Aima Zahid, Joohoon Kim, Taejun Lee, Trevon Badloe, Yeseul Kim, Muhammad Zubair, Kashif Riaz, Muhammad Qasim Mehmood, Junsuk Rho, Photonics Research **9**(9), 09001667 (2021).
[22] Matthew Parry, Andrea Mazzanti, Alexander Poddubny, Giuseppe Della Valle, Dragomir N. Neshev, Andrey A. Sukhorukov, Advanced Photonics **3**(5), 055001 (2021).
[23] Ai Du, Yi Ma, Mingfang Liu, Zhihua Zhang, Guangwei Cao, Hongwei Li, Ling Wang, Peijian Si, Jun Shen, Bin Zhou, High Power Laser Science and Engineering **9**(2), 02000e14 (2021).
[24] Tina Ebert, René Heber, Torsten Abel, Johannes Bieker, Gabriel Schaumann, Markus Roth, High Power Laser Science and Engineering **9**(2), 02000e24 (2021).
[25] Xinhua Xie, Yunpei Deng, Steven L. Johnson, High Power Laser Science and Engineering **9**(4), 04000e66 (2021).
[26] J. Zhang, H. Zhang, W. Yang, K. Chen, X. Wei, Y. Feng, R. Jin, W. Zhu, Advanced Optical Materials **8**, 2000683 (2020).
[27] X. Bai, F. Kong, Y. Sun, F. Wang, J. Qian, X. Li, A. Cao, C. He, X. Liang, R. Jin, W. Zhu, Advanced Optical Materials **8**, 2000570 (2020).
[28] X. Jing, X. Gui, P. Zhou, Z. Hong, Journal of Lightwave Technology **36**(12), 2322 (2018).
[29] R. Xia, X. Jing, X. Gui, Y. Tian, Optical Materials Express **7**(3), 977 (2017).
[30] M. R. Akram, M. Q. Mehmood, X. Bai, R. Jin, M. Premaratne, W. Zhu, Advanced Optical Materials **7**, 1801628 (2019).
[31] M. R. Akram, X. Bai, R. Jin, G. A. E. Vandenbosch, M. Premaratne, W. Zhu, IEEE Transactions on Antennas and Propagation **67**(7), 4650 (2019).
[32] J. Zhao, X. Jing, W. Wang, Y. Tian, D. Zhu, G. Shi, Optics & Laser Technology **95**, 56 (2017).
[33] Y. Tian, X. Jing, H. Gan, X. Li, Z. Hong, Front. Phys. **15**, 62502 (2020).
[34] C. Zhou, Z. Mou, R. Bao, Z. Li, S. Teng, Front. Phys. **16**, 33503 (2021).
[35] G. Dai, Front. Phys. **16**, 53301 (2021).
[36] L. Lan, Y. Gao, X. Fan, M. Li, Q. Hao, T. Qiu, Front. Phys. **16**, 43300 (2021).
[37] J. Li, R. Jin, J. Geng, X. Liang, K. Wang, M. Premaratne, W. Zhu, IEEE Transactions on Antennas and Propagation **67**(4), 2442 (2019).

[38] X. Lu, X. Zeng, H. Lv, Y. Han, Z. Mou, C. Liu, S. Wang, S. Teng, Nanotechnology **31**, 135201 (2020).
[39] H. Lv, X. Lu, Y. Han, Z. Mou, C. Zhou, S. Wang, S. Teng, New J. Phys. **21**, 123047 (2019).
[40] B. Fang, D. Feng, P. Chen, L. Shi, J. Cai, J. Li, C. Li, Z. Hong, X. Jing, Front. Phys. **17**, 53502 (2022).
[41] Vuthy Chheang, Tae-Kyeong Lee, Geum-Yoon Oh, Hong-Seung Kim, Byeong-Hyeon Lee, Doo Gun Kim, Young-Wan Choi, Opt. Express **21**, 20880 (2013).
[42] X. Gao, J. Hui Shi, X. Shen, H. Ma, W. Jiang, L. Li, T. Cui, Applied Physics Letters **102**(15), 151912 (2013).
[43] J. Shibayama, J. Yamauchi, H. Nakano, Electronics Letters **51**(4), 352 (2015).
[44] Weien Lai, Norman Born, Lorenz Maximilian Schneider, Arash Rahimi-Iman, Jan C. Balzer, Martin Koch, Opt. Mater. Express **5**, 2812 (2015).
[45] S. Liu, T. J. Cui, L. Zhang, Q. Xu, Q. Wang, J. G. Han, Adv. Sci. **3**(10), 1600156 (2016).
[46] Hewei Zhao, Shaojia Liu, Yan Wei, Yonghai Yue, Mingrui Gao, Xiaolong Zeng, Xuliang Deng, A. Nicholas, V. Koto, Lin Guo, Lei Jiang, Science **375**(6580), 551 (2022).
[47] Yonghai Yue, Yufei Gao, Wentao Hu, Bo Xu, Jing Wang, Xuejiao Zhang, Qi Zhang, Yanbin Wang, Binghui Ge, Zhenyu Yang, Zihe Li, Pan Ying, Xiaoxiao Liu, Dongli Yu, Bin Wei, Zhong Chang Wang, Xiang-Feng Zhou, Lin Guo, Yongjun Tian, Nature **582**(7812), 370 (2020).
[48] Jianxin Kang, Xiaoyi Qiu, Qi Hu, Jun Zhong, Xiang Gao, Rong Huang, Chengzhang Wan, Li-Min Liu, Xiangfeng Duan, Lin Guo, Nature Catalysis **4**, 1050 (2021).
[49] Ke Chen, Xuke Tang, Binbin Jia, Cezhou Chao, Yan Wei, Junyu Hou, Leiting Dong, Xuliang Deng, Ting-Hui Xiao, Keisuke Goda, Lin Guo, Nature Materials **21**(10), 1121 (2022).
[50] Jianxin Kang, Yufeng Xue, Jie Yang, Qi Hu, Qinghua Zhang, Lin Gu, Annabella Selloni, Li-Min Liu, Lin Guo, Journal of the American Chemical Society **144**(20), 5969 (2022).
[51] Jianwei Nai, Yu Tian, Xin Guan, Lin Guo, Journal of the American Chemical Society **135**(43), 16082 (2013).
[52] Hewei Zhao, Yujie Zhu, Fengshi Li, Rui Hao, Shaoxiong Wang, Lin Guo, Angewandte Chemie International Edition **56**(30), 8766 (2017).
[53] Zhi Cai, Lidong Li, Youwei Zhang, Zhao Yang, Jie Yang, Yingjie Guo, Lin Guo, Angewandte Chemie International Edition **58**(13), 4189 (2019).

*Corresponding authors: hanjunlingjinan@163.com